Impact of shear-thinning and yield-stress drops on solid substrates

G German and V Bertola

School of Engineering, University of Edinburgh, Edinburgh, UK

Abstract
The behaviour of shear-thinning and viscoplastic fluid drops impacting on solid substrates as compared with that of Newtonian drops is studied experimentally by means of high-speed imaging. In particular, the investigation focuses on the morphological aspects of drops after inertial spreading. While the impact morphology of drops of shear-thinning fluids turns out to be qualitatively similar to that of Newtonian fluids, viscoplastic drops can exhibit central drop peaks at the end of inertial spreading. The influence of yield-stress magnitude on drop impact behaviour is qualitatively established by measuring the size of these central drop peaks. The peaks indicate that drop deformation during impact is localized: within a threshold radius, shear-stress effects will not be large enough in magnitude to overcome yield-stress effects, and therefore viscoplastic fluids within this region will not deform from the drop shape prior to impact.

1. Introduction

The phenomenon of a liquid drop impacting on a solid surface is not only an interesting phenomenon commonly observed in nature, it is also an integral component of many applications including the delivery of agrochemicals and pharmaceuticals, spray coating, ink-jet printing, fire suffocation or extinguishment, and the fabrication of micro-lenses [1]. Extensive literature on the dynamics of impacting and spreading Newtonian fluid drops can be found [2–5].

It has been well established that the behaviour of drop impacts varies both with the properties of the fluid and the substrate characteristics. The impact process can be divided into two regimes; an inertial expansion phase and a retraction phase, as shown in figure 1. Upon impact, drops spread due to inertial forces and can form a thin disk called a lamella. During this expansion phase, kinetic energy is converted into capillary energy via the creation of additional drop surface area. Not all the energy is converted however; some is dissipated through viscous effects and some remains as vortical flows near to the lamella rim [6].

Typically drop impact behaviour can be characterized by dimensionless numbers; the most commonly used numbers characterize competition between inertial and capillary forces, represented by the non-dimensional Weber number, $We = \rho v_z^2 D_E/\sigma$ and the competition between inertial and viscous forces, represented by the Reynolds number, $Re = \rho v_z D_E/\mu$ where ρ is the fluid density, v_z is the impact velocity normal
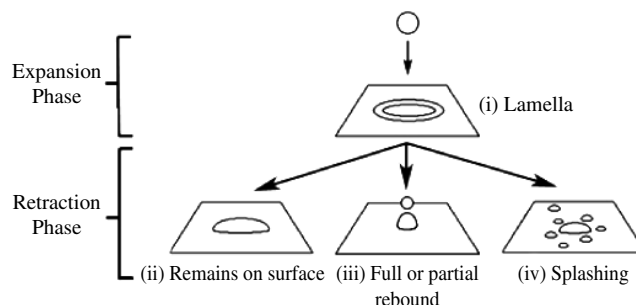

Figure 1. The varied behaviour of drops impacting on a solid surface.

to the substrate, D_E is the drop diameter, σ is the fluid surface tension and μ is the fluid viscosity. Sometimes viscous dissipation is taken into account using the Ohnesorge number $Oh = \sqrt{We/Re}$. Capillary forces drive retraction after a maximum inertial spread has been reached to minimize the free energy of the system. During this retraction phase there is competition between viscous dissipation and capillarity, characterized by the capillary number $Ca = u_x\mu/\sigma$, where u_x is the retraction velocity of the lamella. During this retraction stage, the forces can be strong enough to cause the drop to partially or fully rebound from the surface. Drops of viscous fluid however dissipate rather than convert most of the kinetic energy upon impact, reducing inertial spreading and preventing drops from bouncing off the substrate or splashing.

Table 1. Fluid properties measured at 296 K for solutions of glycerol.

Glycerol mass fraction (—)	Density (kg m^{-3})	Viscosity (Pa s) error $\pm$ 0.005	Surface tension[a] (N m^{-1}) error = $\pm$0.004	Abbreviations used in figure captions
0.98	1256	0.925	0.069	GL098
0.96	1251	0.631	0.069	GL096
0.94	1248	0.428	0.069	GL094
0.9	1236	0.213	0.069	GL090
0.8	1211	0.056	0.070	GL080

[a] Measured on a Kruss EasyDyne surface tensiometer using a Du Nouy ring method.
Errors are based on the correct reading of de-ionized water at 296 K.

More recently, a number of studies about the impact morphology of drops of complex fluids appeared in the literature [7–13]. While most of these works concern the impact of viscoelastic drops, such as dilute solutions of flexible polymers, comparatively little attention has been paid to the investigation of drops of yield-stress (or viscoplastic) fluids [13]. The application of a shear-stress above a threshold value (which is called the yield-stress) causes a viscoplastic fluid to behave like a liquid, however when the applied shear-stress falls below this threshold, the liquid behaves like an elastic solid. A well established and commonly used constitutive equation for viscoplastic fluids is the Herschel–Bulkley model [14], which can be written in the form:

$$\mu = \frac{\tau_c}{\dot{\gamma}} + K\dot{\gamma}^{n-1} \qquad (1)$$

where $\dot{\gamma}$ is the shear rate, τ_c is the yield-stress, K and n are called 'consistency coefficient' and 'power law index', respectively. The latter two parameters are constants which characterize the degree of fluid shear-thinning.

A recent study [13] has investigated the morphology of vaseline drops (which exhibit a measurable yield-stress) impacting on a plexiglass surface. Drop shapes after detachment from a flat-ended needle were found to be initially prolate and decrease in height during a free-fall period of 60 ms. The results indicate that drop shapes tend towards a non-spherical equilibrium state, although this is not explicitly stated. A threshold value of the Bingham number:

$$Bm = \frac{\tau_c D_E}{\mu_0 v_z} \qquad (2)$$

which characterizes the competition between yield-stress and viscous forces, was also established below which the maximum inertial spreading diameter at the end of the inertial expansion phase was smaller than the final sessile drop diameter after spreading. The viscosity term μ_0 in this study was taken to be the low shear rate finite viscosity term of the Cross model constitutive equation [15]:

$$\mu(\dot{\gamma}) = \mu_1 + \frac{(\mu_0 - \mu_1)}{[1 + (C\dot{\gamma})^{1-m}]} \qquad (3)$$

where C in equation (3) is the cross time constant, $(1 - m)$ is the rate constant and μ_1 is the high shear rate finite dynamic viscosity. This relationship is somewhat ambiguous however because vaseline exhibits both yield-stress and shear-thinning

characteristics; the viscosity therefore varies with shear-stress during drop impact and cannot be simply characterized in terms of the viscosity at low shear-rates. Thus, in order to identify the effects of the yield-stress on drop impact one should be able to isolate those of shear-thinning. Furthermore, the Bingham number does not account for capillary forces, which along with the surface energy of the substrate influence the equilibrium sessile drop shape.

The present investigation attempts to get a deeper insight of the impact morphology of non-Newtonian drops by comparing the impact morphologies of drops of three different fluids impacting on substrates having different surface energies. In particular, this work compares: (i) Newtonian drops of variable viscosity; (ii) purely shear-thinning drops; (iii) yield-stress drops. In fact, whilst the influence of the fluid viscosity, the Weber number and the surface wettability on drop impact have all previously been investigated in detail, the effects of fluid shear-thinning and yield-stress remain relatively unknown to date. The results establish a relationship between the yield-stress magnitude and the drop impact morphology and develop existing studies into the influence of surface wettability on drop impact dynamics [16–19] to incorporate more viscous Newtonian fluids as well as shear-thinning and viscoplastic fluids.

2. Experimental apparatus, methods and materials

2.1. Fluid characterization

Five Newtonian fluid solutions, ranging in viscosity between 0.056 Pa s $\leqslant \mu \leqslant$ 0.925 Pa s, were prepared by dissolving glycerol, with mass fractions 0.98, 0.96, 0.94, 0.9 and 0.8 in de-ionized water. Each solution was mixed for approximately 2 h to ensure homogeneity using a magnetic stirrer and then re-stirred before use. Table 1 displays the fluid properties of each solution.

Viscosity measurements for the Newtonian, shear-thinning and yield-stress fluids were measured using a controlled rate (CR) test across the shear rate range 0 s^{-1} $\leqslant$ $\dot{\gamma} \leqslant$ 100 s^{-1} using a Haake–Mars rotational rheometer with a cone-and-plate configuration (35 mm diameter, 2° gap angle).

Four shear-thinning fluids were prepared by dissolving xanthan gum with mass fractions 0.001 25, 0.0025, 0.005 and 0.01 in de-ionized water. The solutions, none of which exhibit yield-stress characteristics, were prepared by slowly adding the xanthan gum to de-ionized water whilst continuously

Table 2. Fluid properties measured at 296 K for aqueous solutions of xanthan gum including and power law model fitted parameters n and K.

Xanthan gum mass fraction (—)	Density (kg m^{-3})	Surface tension[a] (N m^{-1})	Consistency coefficient K (Pa s^n)	Power law index n (—)	Abbreviations used in figure captions
0.001 25	1000	0.071 ± 0.0015	0.208 ± 0.001	0.400 ± 0.003	X0125
0.0025	1000	0.071 ± 0.0001	0.962 ± 0.006	0.155 ± 0.005	X025
0.0050	1000	0.070 ± 0.0008	2.846 ± 0.015	0.129 ± 0.004	X05
0.0075	1000	0.072 ± 0.0012	5.064 ± 0.027	0.084 ± 0.005	X075

[a] Measured on a Kruss EasyDyne surface tensiometer using a Du Nouy ring method. Errors are based on the standard deviation of five samples for each shear-thinning fluid solution.

Table 3. Fluid properties, measured yield-stress and Herschel Bulkley model fitted parameters n and K for yield-stress fluid solutions at 296 K.

Hair-gel mass fraction (—)	Density (kg m^{-3})	Surface tension[a] (N m^{-1})	Measured yield-stress, τ_c (Pa)	Consistency coefficient K (Pa s^n)	Power law index n (—)	Abbreviations used in figure captions
0.2	1037	0.034 ± 0.0008	0	1.4425 ± 0.009	0.4747 ± 0.005	YSF020
0.25	1047	0.034 ± 0.0008	5.4 ± 0.6	3.096 ± 0.019	0.4311 ± 0.007	YSF025
0.3	1057	0.034 ± 0.0015	11.5 ± 1.3	5.533 ± 0.015	0.3775 ± 0.004	YSF030
0.35	1067	0.034 ± 0.0024	19.1 ± 0.7	6.982 ± 0.030	0.373 ± 0.005	YSF035
0.4	1076	0.034 ± 0.0031	26.1 ± 1.8	7.936 ± 0.033	0.3727 ± 0.004	YSF040
0.45	1086	0.0340 ± 0.0040	32.7 ± 0.9	12.048 ± 0.039	0.3579 ± 0.007	YSF045
0.5	1096	0.0340 ± 0.0041	36.2 ± 1.9	19.925 ± 0.051	0.3116 ± 0.006	YSF050

[a] Measured on a Kruss EasyDyne surface tensiometer using a Du Nouy ring method. Errors are based on the standard deviation of ten samples.

swirling the fluid in order to disperse the powder and avoid agglomeration. The solutions were then mixed using a magnetic stirrer for 2 h and re-stirred before each use. Each fluid sample was used within 48 h to avoid changes in viscometric characteristics due to bacterial degradation. The fluid properties of each solution are detailed in table 2.

To characterize each fluid solution, rheological measurements were fitted with a power law model [20] with the constitutive equation:

$$\mu = K\dot{\gamma}^{n-1}. \qquad (4)$$

Table 2 displays these fitted parameters for each solution.

Model yield-stress fluids were obtained using a commercial polymer-based hairdressing gel, which contains a mixture of alcohol, water, carbomers, surfactants and glycerin and mixes readily with water. Seven solutions were prepared by dissolving the gel in de-ionized water, with mass fractions 0.2, 0.25, 0.3, 0.35, 0.4, 0.45 and 0.5. The solutions were mixed slowly in a container to avoid the formation of bubbles, left to settle for 24 h and then thoroughly mixed to ensure homogeneity using a magnetic stirrer. The fluid properties of each solution are detailed in table 3.

The viscosities of certain complex fluids are difficult to measure at low shear-rates and there is current debate [21, 22] over whether it is entirely accurate to define a fluid as having a yield-stress. Irrespective of the semantics of the argument however, the research presented here recognizes that the rheological properties of viscoplastic fluids can be well represented by a real and measurable yield-stress component.

The yield-stress magnitude of each solution was determined by performing a controlled stress (CS) test on a Haake–Mars rotational rheometer using a plate-and-plate configuration with the surfaces covered with sandpaper to avoid slip.
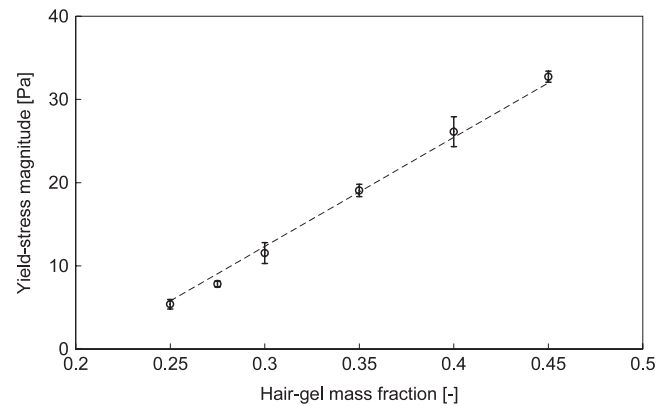

Figure 2. Variation of fluid yield-stress magnitude τ_c with hair-gel mass fraction.

Measurements were made within the range 0 Pa $\leqslant \tau \leqslant$ 50 Pa. The fluid yield-stress magnitude was found to vary as a linear function of the solution concentration, as shown in figure 2.

Yield-stress fluids also exhibit shear-thinning characteristics after flow commencement. The viscometric properties of each fluid solution were fitted using a Herschel–Bulkley model (equations (1)) to characterize this behaviour. Table 3 displays the fitted model parameters for each solution.

The surfactant Polysorbate 20 is present in each of the viscoplastic fluid solutions with concentrations significantly higher than the critical micelle concentration (C.M.C.). Surface tension measurements of each solution in table 3 are in good agreement with previous measurements [23] of Polysorbate 20 in de-ionized water ($\sigma = 0.036$ N m^{-1})
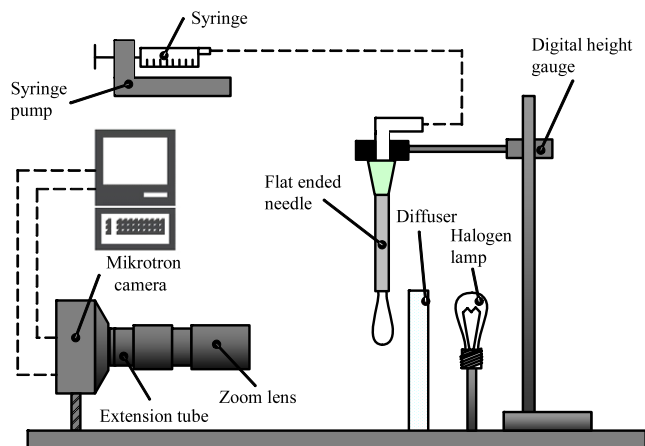
Figure 3. Drop generation and image capturing equipment.

for concentrations at and above the C.M.C. (0.06 mg ml^{-1}). Dynamic surface tension effects that may be important over the short timescales of drop impact ($\sim$5 ms) were considered not to be influential. In fact, fluids with surfactant concentrations well above the C.M.C. show demicellization (i.e., a breaking up of micelles into their constituent surfactant molecules) in response to non-equilibrium conditions during inertial spreading (from surfactants being diluted at newly formed surfaces). Demicellization responds nearly immediately to drop deformation, resulting in a dramatic decrease in dynamic surface tension effects by way of increasing the rate at which surfactant molecules reach newly formed surface regions [24, 25]. The surface tension of the viscoplastic fluids was therefore assumed constant.

2.2. Experimental apparatus

The experimental apparatus is schematically shown in figure 3. Drops are produced at the end of a 1.27 mm O.D, 0.838 mm I.D. (Needle gauge 18) flat-ended hypodermic needle attached to a screw driven syringe dispenser and allowed to detach under their own weight. The needle is centred over an aluminium square block (40 mm × 40 mm) upon which a substrate is placed. For the current investigation, impacts were examined on a parafilm-M (typical surface roughness: 42–51 nm [26]) and a clean glass substrate (typical surface roughness: 15 nm [27]), which are characterized by different surface energies. Changes in impact velocity are achieved by varying the fall height using a Vernier height gauge with a precision of ±0.01 mm. Drop impacts are examined at fall heights of H_f = 7.5, 10, 25, 50, 100 and 200 mm, corresponding to a Weber number range $1.7 \leqslant We \leqslant 240$ for the Newtonian solutions, $0.8 \leqslant We \leqslant 193$ for the shear-thinning fluids and $0.7 \leqslant We \leqslant 340$ for the yield-stress fluids.

The surface energy of each substrate was characterized using the equilibrium contact angle, θ_e, of a drop of de-ionized water (D_E = 3.48 mm, σ = 0.076 N m^{-1}). For the parafilm-M substrate, the average contact angle of five drop measurements gives θ_e = 95° ± 2°; the glass substrate was found to be completely wetting (θ_e = 0°).

Table 4. Drop mass, capillary length and equivalent drop diameter measurements.

Fluid abbreviation	Average drop mass (mg)	Measurement error (mg)	D_E (mm)	Standard deviation (mm)	Capillary length a (mm)
GL098	19.6	0.3	3.10	0.006	2.78
GL096	19.8	0.3	3.12	0.006	2.37
GL094	19.5	0.2	3.10	0.003	2.37
GL090	20.1	0.5	3.14	0.008	2.37
GL080	19.5	0.3	3.13	0.005	2.39
YSF020	12.1	0.2	2.85	0.006	2.43
YSF025	10.8	0.3	2.74	0.009	1.83
YSF030	10.1	0.3	2.68	0.009	1.82
YSF035	9.6	0.3	2.64	0.005	1.81
YSF040	9.4	0.4	2.62	0.005	1.80
YSF045	9.4	0.2	2.62	0.016	1.79
YSF050	9.2	0.2	2.60	0.015	1.79
X0125	22.0	0.3	3.48	0.017	1.78
X025	20.5	0.6	3.40	0.032	2.69
X05	21.1	0.1	3.42	0.007	2.69
X075	19.6	0.1	3.35	0.007	2.67

Drop impact and free-fall characteristics were observed using a high frame rate Mikrotron MC1311 camera, equipped with a Sony 18–108 mm/f2.5 zoom lens. Back to front illumination was provided using a fluorescent lamp equipped with a diffuser. Digital images were recorded at 1000 frames s^{-1} with an image resolution of 720 pixels × 512 pixels. The magnification was manipulated so that the image accommodated the maximum spread of the impacting drop with a typical spatial resolution of 32.6 μm/pixel. The magnification was kept constant throughout all experiments and lengths on the image could be calculated by comparison with a reference length (the width of the needle). Vibrational isolation and fine optical alignment was achieved by attaching the apparatus to an optical bench.

2.3. Drop production and characterization

Drop diameters are measured by averaging the drop mass of each fluid solution over 50 samples using a precision balance and substituting into $D_E = \sqrt[3]{6m/\pi\rho}$, where m is the average drop mass and ρ is the fluid density. D_E represents the equivalent spherical drop diameter. This method is used instead of directly measuring dimensions from the recorded digital images because drops oscillate during free-fall and some viscoplastic drops do not assume an equilibrium spherical form. The average drop mass and D_E for each solution is detailed in table 4. Whereas the drop diameters of the Newtonian fluids in the range 0.056 Pa s $\leqslant \mu \leqslant$ 0.925 Pa s do not vary significantly (D_E = 3.118 ± 0.016 mm), shear-thinning drop diameters vary as a linear function of the xanthan gum mass fraction X and is well represented by

$$D_E = 3.480 - 16.483X. \tag{5}$$

Viscoplastic drop diameters also vary as a linear function of the hair-gel mass fraction, Y, and are well represented by
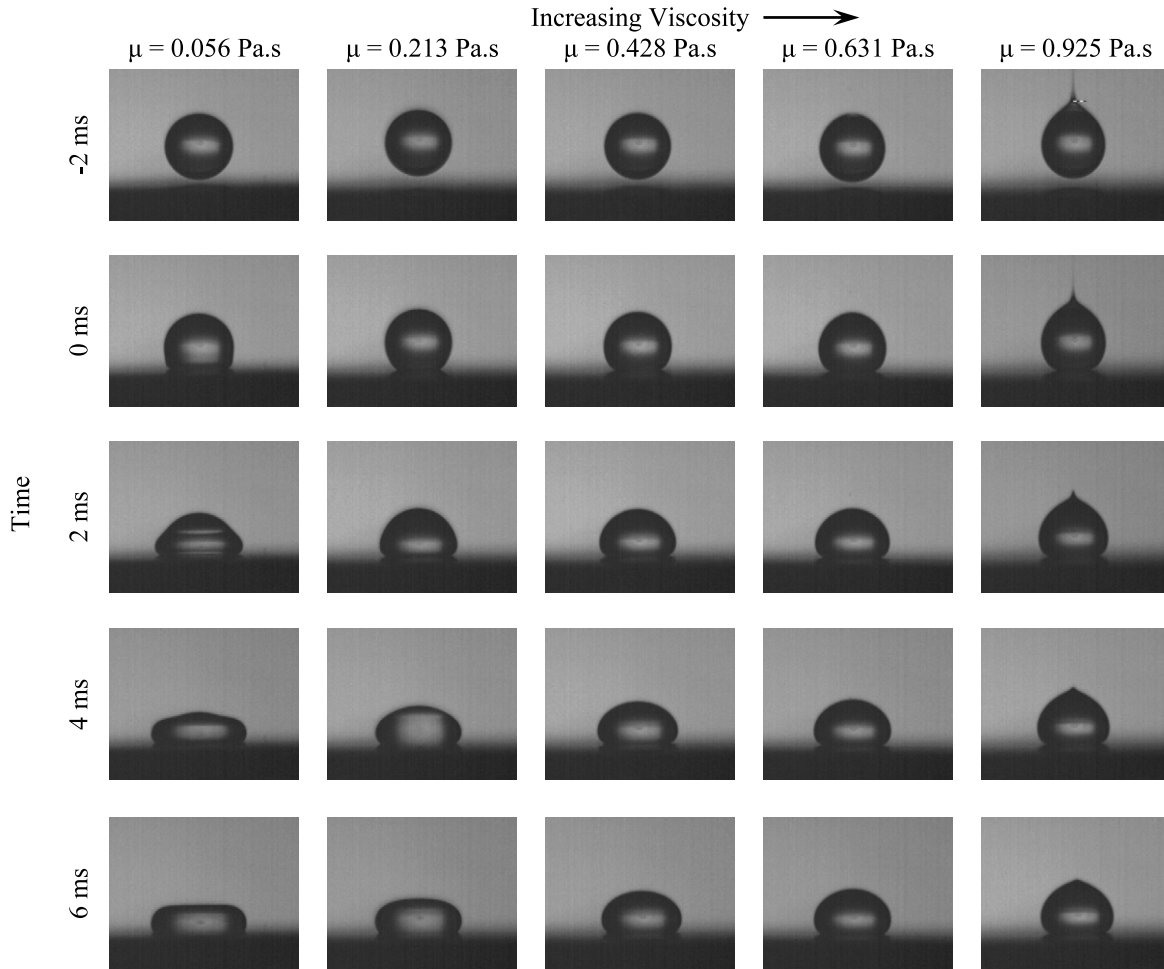
$$D_E = 3.059 - 1.222Y. \tag{6}$$

Figure 4. The parametric morphology of viscous Newtonian fluid drops impacting on a parafilm substrate from a fall height of 10 mm.

To characterize the shape of the drops deposited on a solid surface, comparisons of the drop radius were made with the capillary length $a = \sqrt{\sigma/\rho g}$, which characterizes the competition between capillary forces and gravity. The capillary lengths were found to be larger than the drop radius ($D_E/2$) for each fluid solution, as detailed in table 4. This indicates that sessile drops in the absence of any inhibiting forces will take on a spherical cap shape.

The impact velocity was measured directly from digital images of falling drops. Within the range of free-fall heights ($7.5 \text{ mm} \leqslant H_f \leqslant 200 \text{ mm}$) measurements agree closely with the theoretical free-fall velocity, $u_z = \sqrt{2g(H_f - D_E)}$.

3. Results and discussion

Figures 4 and 7 show image sequences of Newtonian drop impacts (with $0.056 \text{ Pa s} \leqslant \mu \leqslant 0.925 \text{ Pa s}$) on a parafilm-M surface from a fall height of 10 and 100 mm. Equivalent impacts for shear-thinning drops with $0.084 \leqslant n \leqslant 0.4$ and $0.208 \text{ Pa s}^n \leqslant K \leqslant 5.064 \text{ Pa s}^n$ (figures 5 and 8) and yield-stress fluid drops (figures 6 and 9) with $0 \text{ Pa} \leqslant \tau_c \leqslant 26.1 \text{ Pa}$ are also displayed.

The influence of impact velocity can clearly be observed from the image sequences in figures 4–9. For each fluid type,

the maximum spread factor $\beta_m = D_{Max}/D_E$ and minimum apex height factor $\xi_m = h_{Min}/D_E$ during inertial expansion increase and decrease respectively as the impact velocity rises. A decrease in Newtonian fluid viscosity in figures 4 and 7 also has a similar influence; lower viscosity fluids reach a larger maximum diameter with the lamella appearing much thinner. The expansion phase time (from impact to maximum spreading) also decreases as a function of the impact velocity for each of the fluid solutions, from approximately 7 to 4 ms.

Whilst differences in impact dynamics between the different shear-thinning fluids are noticeable from the image sequences in figures 5 and 8, it is not immediately obvious how the consistency coefficient K and the power law index n independently influence dynamic behaviour. Increases in β_m and decreases in ξ_m are observed for decreases in xanthan gum mass fraction (increasing n and decreasing K).

The drop impact dynamics of some yield-stress fluids during the expansion phase (shown in figures 6 and 9) differs significantly from both Newtonian and shear-thinning fluids. For fluids with $\tau_c < 11.5 \text{ Pa}$, the general drop impact behaviour does not appear to vary significantly from that of shear-thinning and Newtonian drops: equilibrium drop shapes just before impact are close to spherical, and increasing the hair-gel mass fraction causes a reduction of β_m and an increase of
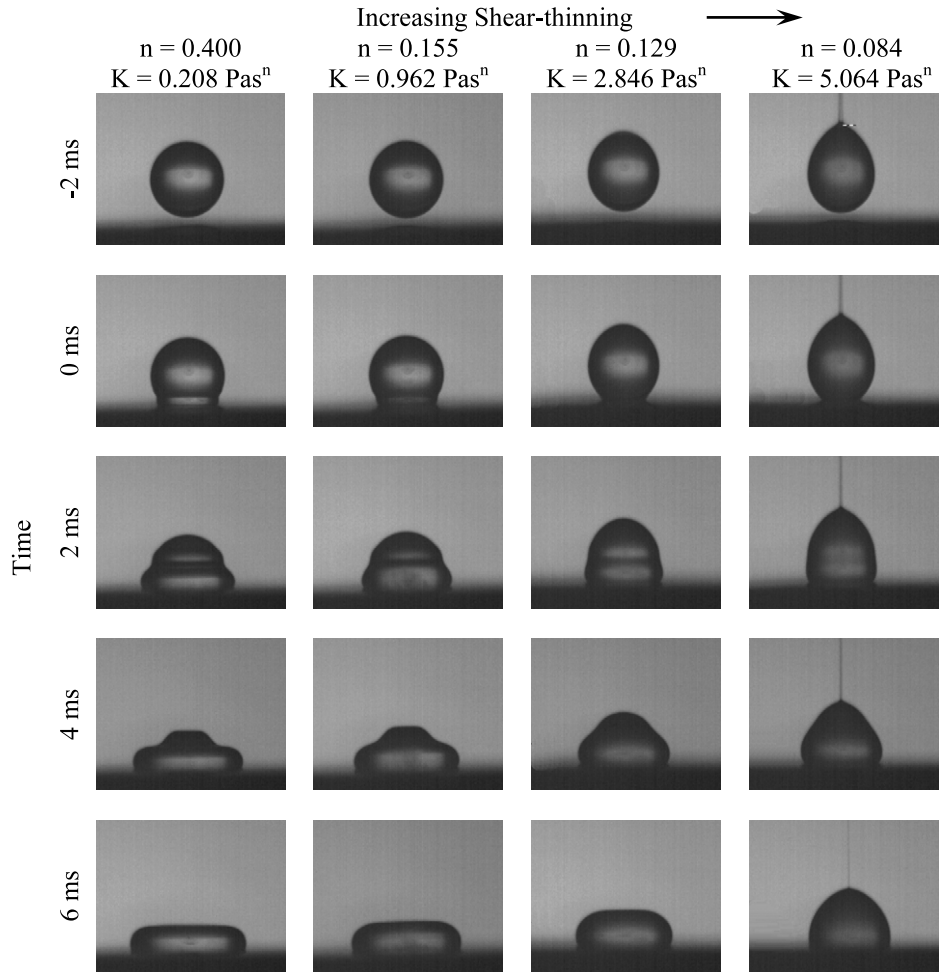
Figure 5. The parametric morphology of shear-thinning fluid drops impacting on a parafilm substrate from a fall height of 10 mm.

ξ_m similar to what happens increasing viscosity in Newtonian drops. However, for $\tau_c \geqslant 11.5$ Pa equilibrium drop shapes during free-fall become increasingly prolate with the yield-stress magnitude τ_c, and do not deform completely upon impact. In particular, at maximum spread drops do not take on a disk-like shape, but central peaks are observed. This suggests that flow is localized during inertial expansion: the upper part of the prolate drop does not deform from its original shape prior to impact, resulting in a characteristic peak. Peaks are most noticeable for low velocity impacts where deformation is small. As the impact velocity increases, the drop peak size decreases and eventually disappears. Peak sizes also appear to increase with τ_c: high τ_c drops, impacting at low Weber numbers, show very little deformation during inertial expansion.

3.1. Influence of surface wettability

Previous studies have reported differences in the maximum spreading diameter β_m at the end of the expansion phase for water drops ($\mu = 0.001$ Pa s) impacting on substrates with different surface energies. Differences of up to 23.6% were measured by Pasandideh–Fard et al [17] for drops (of similar size to the present investigation) impacting on glass ($\theta_e = 27°$)

and beeswax ($\theta_e = 111°$) substrates in the ranges $59 \leqslant We \leqslant 271$ and $2084 \leqslant Re \leqslant 5833$. Differences of 10.4% were measured by Mao et al [18] for similar sized drops impacting on glass ($\theta_e = 37°$) and wax ($\theta_e = 97°$) substrates in the range $11.3 \leqslant We \leqslant 518$ and $1482 \leqslant Re \leqslant 100\,24$. We extend these investigations here by examining the influence of surface wettability on drops of more viscous Newtonian fluids with 0.056 Pa s $\leqslant \mu \leqslant 0.925$ Pa s over the ranges $1.7 \leqslant We \leqslant 240$ and $1.1 \leqslant Re \leqslant 137$, shear-thinning fluids with $0.084 \leqslant n \leqslant 0.400$ and 0.208 Pa s$^n \leqslant K \leqslant 5.064$ Pa s^n over the range $0.8 \leqslant We \leqslant 193$ and viscoplastic fluids with $0.3727 \leqslant n \leqslant 0.4747$, 1.443 Pa s$^n \leqslant K \leqslant 7.936$ Pa s^n and 0 Pa $\leqslant \tau_c \leqslant 26.1$ Pa over the range $0.7 \leqslant We \leqslant 340$. The influence of surface wettability is assessed by comparing equivalent drop impacts on hydrophilic glass and hydrophobic parafilm-M substrates.

Figure 10 displays temporal variations in $\beta = D/D_E$ for impacts of GLY094 ($\mu = 0.428$ Pa s) fluid drops on both parafilm (open symbols) and glass (filled symbols) substrates. Substrate wettability does not appear to significantly influence impact behaviour during the expansion phase, however after β_m is reached, differences become more apparent. Impacts on the parafilm substrate typically show long and slow retraction phases, while impacts on the glass substrate exhibit a short
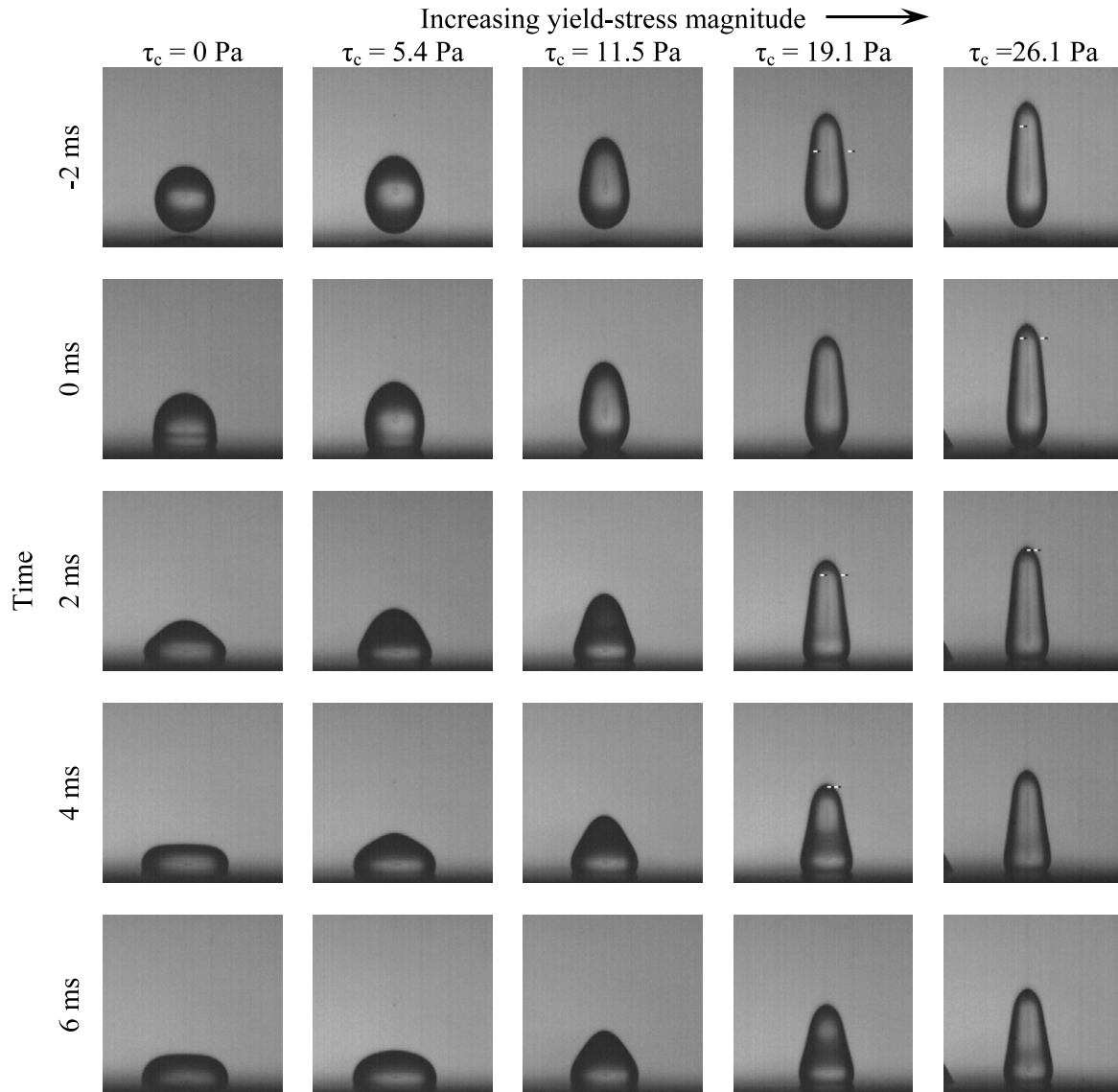
Figure 6. The parametric morphology of yield-stress fluid drops impacting on a parafilm substrate from a fall height of 10 mm.

retraction phases followed by a stage where the drop spreads continuously under the action of capillarity.

At the end of the inertial expansion phase, the measured values of β_m and ξ_m are a function of both the Weber number and viscosity (in particular, they increase and decrease, respectively, with increasing We and decreasing viscosity, as displayed in figures 11 and 12). This is in good agreement with previous observations [16–18, 28, 29]. Unlike the effect of wettability on low viscosity drop impacts (with $\mu \sim 0.001$ Pa s) however, both β_m and ξ_m for fluids with 0.056 Pa s $\leqslant \mu \leqslant$ 0.925 Pa s do not vary significantly with substrate wettability within the ranges $1.7 \leqslant We \leqslant 240$ and $1.1 \leqslant Re \leqslant 137$. This suggests that whilst substrate wettability influences the impact dynamics of low viscosity liquids during the expansion phase, the measurable difference decreases as the viscosity is increased and for Newtonian fluids with $\mu \geqslant 0.056$ Pa s, measured differences fall within experimental error. Moreover, the maximum inertial spread factor of water drops were observed to decrease as the dynamic

contact angle increased by Fukai *et al* [19]. To extend this conclusion accounting for more viscous Newtonian fluids, the advancing contact angle, θ_a, was measured for drops of each solution impacting on the glass and parafilm substrates. θ_a was found to be $135° \pm 10°$ for both substrates. This confirms that differences in θ_a between the two substrates are small for fluids with $\mu \geqslant 0.056$ Pa s and fall within experimental error.

As with the Newtonian fluids, equivalent shear-thinning fluid drop impacts on glass and parafilm substrates are very similar during the inertial expansion phase. This can be observed in figure 13, which plots temporal variations in β for drops of the X050 ($K = 2.846$ Pa s^n, $n = 0.129$) fluid. Noticeable differences can only be observed after maximum inertial spread is reached, whereupon drops on the parafilm surface show significantly larger retraction phases than on the glass surface. Differences in β_m and ξ_m between equivalent drop impacts on the two substrates are small across the range $0.8 \leqslant We \leqslant 193$ in figures 14 and 15 respectively; both β_m and ξ_m results agree to within experimental error, indicating
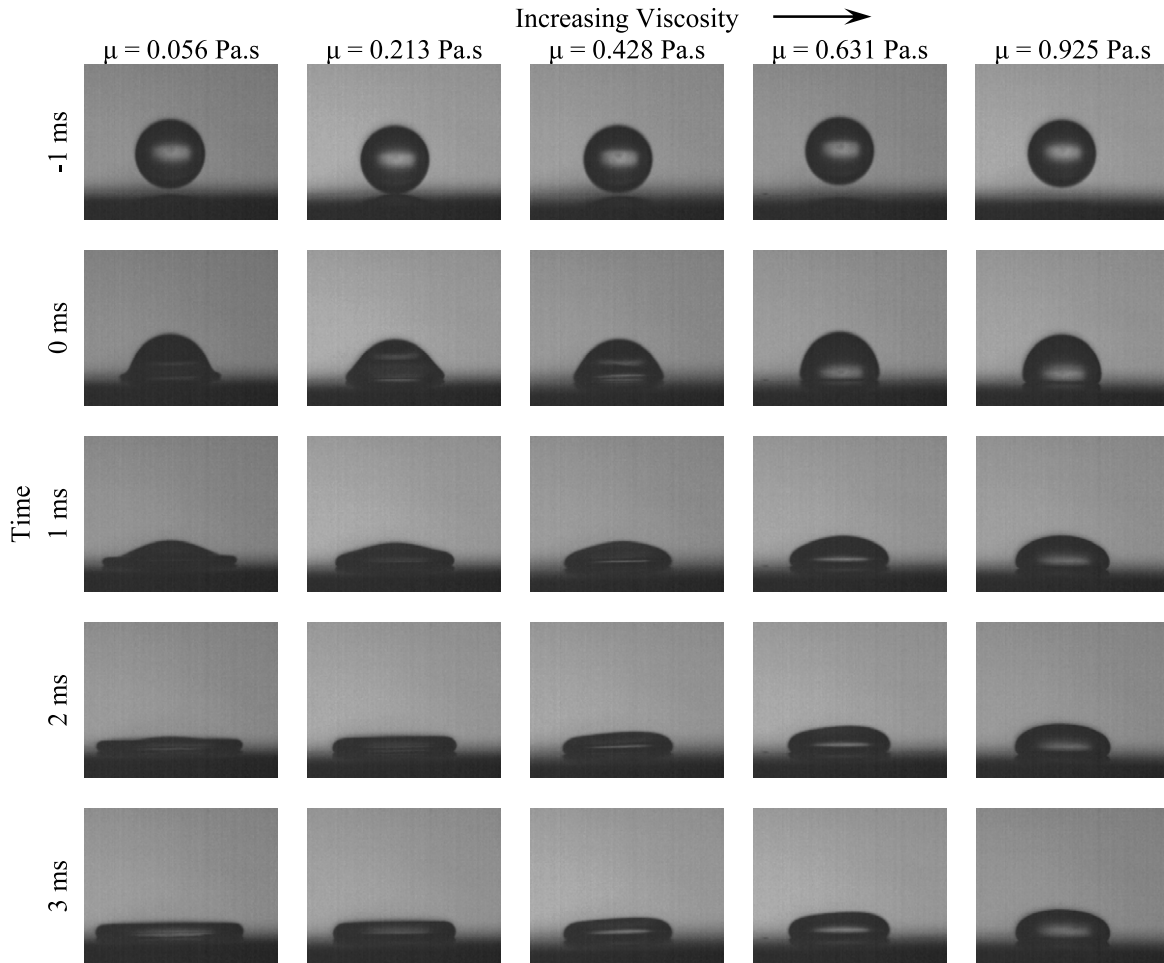
Figure 7. The parametric morphology of viscous Newtonian fluid drops impacting on a parafilm substrate from a fall height of 100 mm.

that the surface energy of the substrate does not appear to influence shear-thinning fluid drop impacts during the inertial expansion phase.

The influence of surface wettability on viscoplastic drop impacts with 0 Pa $\leqslant \tau_c \leqslant$ 26.1 Pa is only noticeable after the end of the inertial expansion stage. This is highlighted in figure 16, which displays temporal variations in β for the YSF030 ($\tau_c = 11.5$ Pa) fluid for impacts on both parafilm and glass substrates from fall heights in the range 10 mm $\leqslant H_f \leqslant$ 200 mm. Viscoplastic fluids exhibiting a measurable yield-stress show only small retraction phases for impacts on parafilm, similar to those observed for high viscosity Newtonian fluids. No significant retraction phase is observed for impacts on glass and slow spreading driven by capillarity follows directly on from inertial expansion.

Figures 17 and 18 respectively compare β_m and ξ_m for equivalent impacts on the parafilm and glass substrates in the range 2.9 $\leqslant We \leqslant$ 340. Both diameter and height results closely agree, with measured differences falling within experimental error for each solution. Fluid yield-stress effects therefore do not contribute to increases in the influence of the surface energy of the substrate. Moreover, the similarity of the results also highlights that the phenomena of slip effects, commonly observed in yield-stress fluid flows [30] are also not significant or equally influential on both substrates.

3.2. Influence of fluid viscosity

The influence of fluid viscosity on drop impact dynamics can be observed in figures 11 and 12: increasing μ reduces the spreading factor, β_m, and increases the dimensionless drop height, ξ_m. Increasing the fluid viscosity increases losses through viscous dissipation during the expansion phase, and consequently reduces the fraction of the impact kinetic energy available for conversion into surface energy, hence β_m decreases. By conservation of volume, the minimum dimensionless height factor ξ_m increases with viscosity. Whilst drop deformation can be significant for low viscosity fluids, drops with a moderately high viscosity ($\mu \geqslant 0.428$ Pa s) can show only small deformations and do not assume a typical disk-like lamella shape upon reaching a maximum impact diameter (figure 4). Instead the shape at maximum inertial spread appears more like a spherical cap.

A majority of existing research into drop impact behaviour focuses predominantly on high We impacts of low viscosity fluids such as water ($\mu = 0.001$ Pa s). From this research numerous empirical and semi-empirical models have been proposed that predict β_m and ξ_m as a function of the Weber, Reynolds and Ohnesorge numbers, and of the equilibrium and advancing contact angles. The accuracy of these models varies considerably, however most contemporary models are
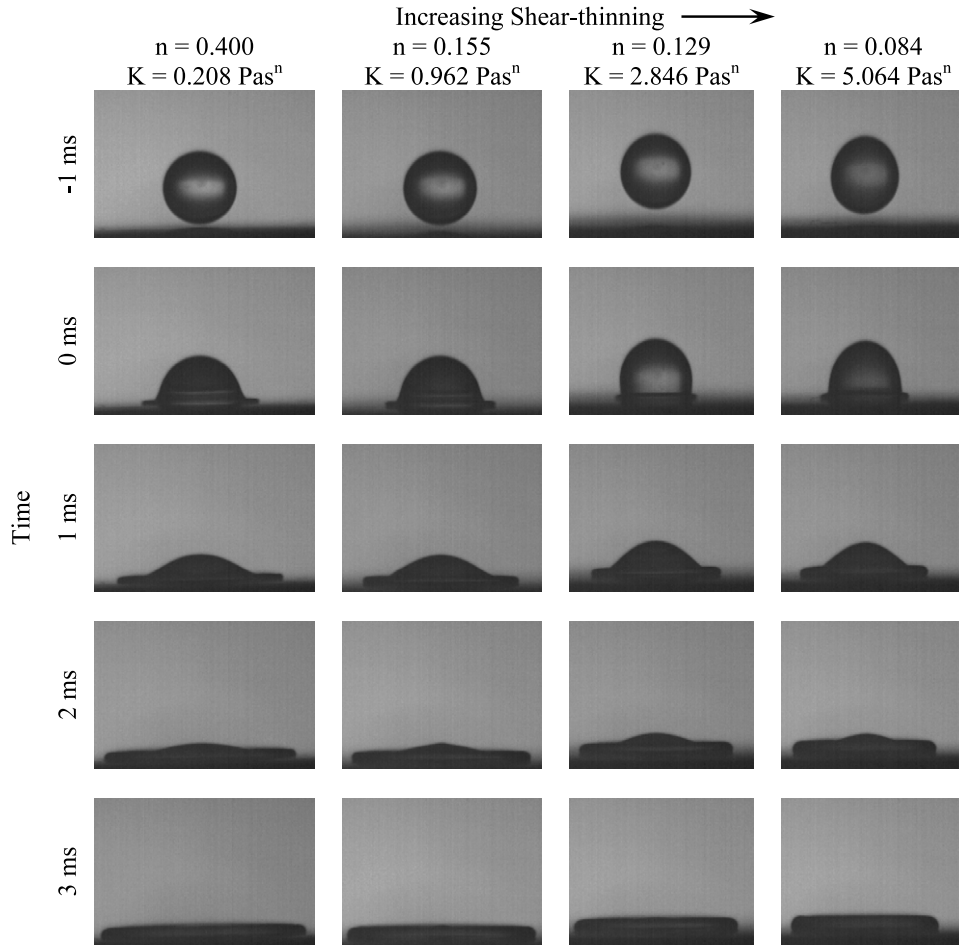
Figure 8. The parametric morphology of shear-thinning fluid drops impacting on a parafilm substrate from a fall height of 100 mm.

based on a simple energy conservation, where the sum of the kinetic and surface tension energies prior to impact are equated to the sum of the surface tension energy and losses through viscous dissipation at the end of the inertial expansion phase. Included in this conservation is a common assumption that drops can be approximated to that of a thin cylinder at the end of inertial spreading. This assumption is limiting however when attempting to predict low We impacts of high viscosity fluids. Experimental measurements were compared with a number of theoretical prediction models [6, 17, 18, 31] and whilst the model by Mao *et al* [18]

$$\left[\frac{1}{4}(1 - \cos\theta) + 0.2\frac{We^{0.83}}{Re^{0.33}} \right]\left(\frac{D_{\mathrm{Max}}}{D_{\mathrm{E}}} \right)^3$$
$$- \left[\frac{We}{12} + 1 \right]\left(\frac{D_{\mathrm{Max}}}{D_{\mathrm{E}}} \right) + \frac{2}{3} = 0 \qquad (7)$$

was found to provide predictions in closest agreement with the experimental results (figure 19), differences of up to ±18% were observed for impacts with $We \geqslant 100$, and up to ±32% for $We \leqslant 50$ [32]. This highlights the limit of this (and most other) energy conservation models, wherein the precision decreases significantly towards lower Weber numbers since the surface tension effects play a more important role in spreading and a flat disk assumption becomes invalid. The predictions

also underestimate measured β_{m} values, suggesting that the model overestimates viscous dissipation losses during impact.

To further investigate the relationship between drop impact dynamics and fluid viscosity towards lower Weber numbers, power law distributions of the form $\beta_{\mathrm{m}} = \mu^{\psi}$ were fitted to the experimental data and re-plotted as a function of μ. The results for β_{m} are shown in figure 20.

For $We \sim 211$, $\psi = -1/6$: this value is close the classical scaling law relationship, $\beta_{\mathrm{m}} = Re^{1/5}$ established by Chandra and Avedisian and highlighted by Clanet *et al* [6]. However, as the Weber number decreases, one can observe that the absolute value of the exponent ψ becomes smaller and smaller. For $2.6 \leqslant We \leqslant 4.8$, ψ varies between $-1/11$ and $-1/14$. This indicates that the relative importance of μ on β_{m} diminishes as the Weber number is reduced; an expected result given that regardless of fluid viscosity, the maximum spread of a drop will tend towards an undeformed state as the Weber number tends to zero and inertial expansion becomes increasingly small.

3.3. Influence of shear-thinning

The influence of shear-thinning on drop impact behaviour can be observed in figure 21, which plots temporal variations of β and ξ for the four shear-thinning fluids, for impacts at

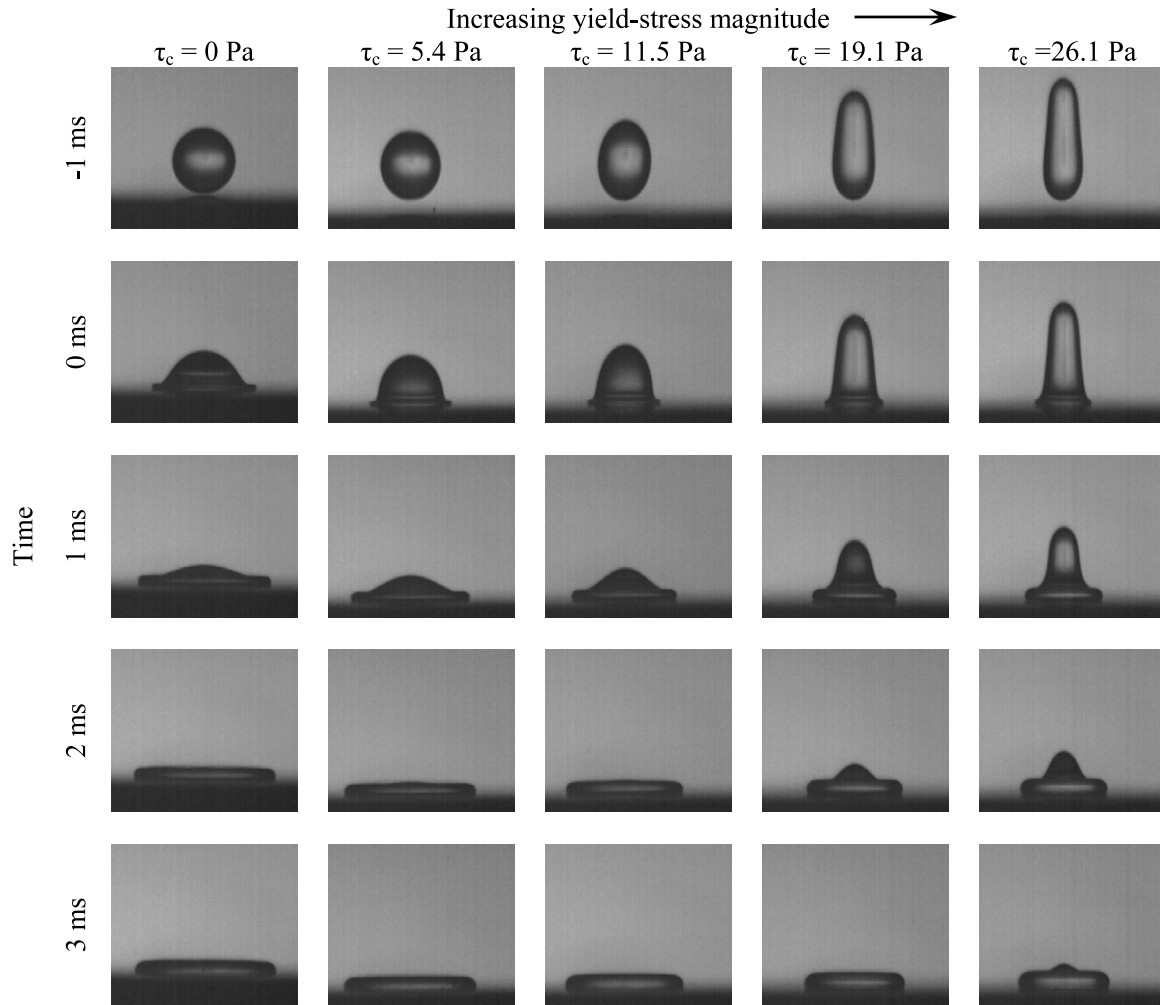Increasing yield-stress magnitude $\longrightarrow$

Figure 9. The parametric morphology of yield-stress fluid drops impacting on a parafilm substrate from a fall height of 100 mm.

$We = 43.2 \pm 1.4$ ($H_\mathrm{f} = 50$ mm) on a parafilm substrate. Unlike Newtonian drops, which are characterized simply by viscosity, the behaviour of drops of shear-thinning fluids is more complex, and even using the simple power law model given by equation (4) is characterized by two parameters, the consistency coefficient K and power law index n.

Increasing the mass fraction of xanthan gum increases the consistency coefficient K, however it also decreases the power law index n. In other words, fluids both become more viscous at low shear-rates and more shear-thinning with increases in mass fraction. Increasing the mass fraction has the effect of decreasing β_m, whilst ξ_m for each fluid remains very similar, indicative of thin cylindrical lamella formation (where variations in drop height with the Weber number are small).

Unfortunately, the fluids used in the present work do not allow one to establish the independent influence of K and n on the impact behaviour by direct experimental comparison because fluids with identical values of K and different power law indices cannot be produced. The results from figures 14 and 15 can however suggest what effect each parameter K and n has on impact behaviour. In fact, for two identical fluid drops (equal ρ, σ and D_E) with equal values of K and differing power law indices subject to equivalent impacts, the fluid exhibiting
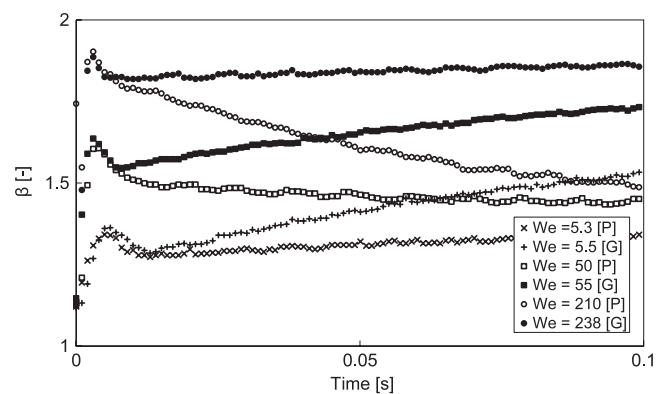

Figure 10. Dimensionless drop diameter β plotted against time for drops of the GLY094 Newtonian fluid ($\mu = 0.428$ Pa s) impacting from fall heights of 10 ($We \sim 5$), 50 ($We \sim 50$) and 200 mm ($We \sim 220$) on glass [G] ($\theta_\mathrm{e} = 0°$, solid symbols) and parafilm-M [P] ($\theta_\mathrm{e} = 95 \pm 2°$, open symbols) substrates.

the greatest degree of shear-thinning (i.e., n closest to 0) would be expected to exhibit lower local viscosities during inertial expansion and therefore increased β_m. On the contrary,
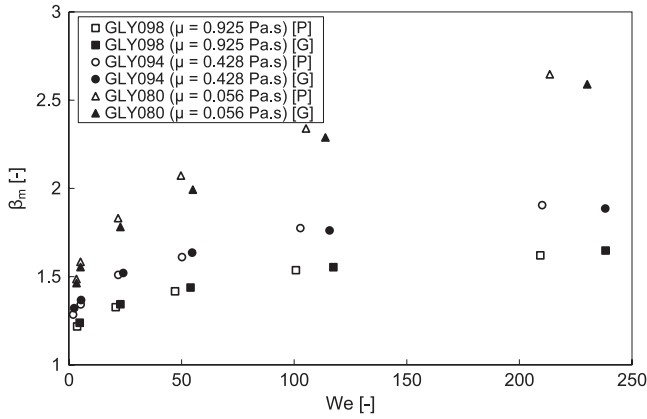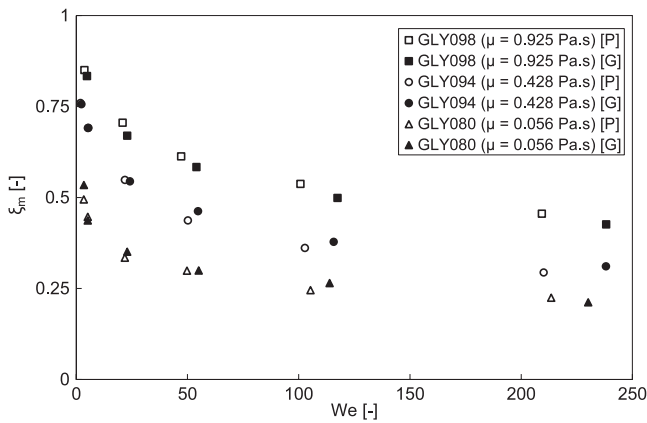
Figure 11. Comparison of maximum dimensionless spread factor β_m for Newtonian fluid drops GL098 ($\mu = 0.925$ Pa s, $D_E = 3.102$ mm), GL094 ($\mu = 0.428$ Pa s, $D_E = 3.101$ mm) and GLY080 ($\mu = 0.056$ Pa s, $D_E = 3.133$ mm) impacting on parafilm [P] ($\theta_e = 95 \pm 2°$, open symbols) and glass [G] ($\theta_e = 0°$, solid symbols) substrates. Errors are predominantly comparable to the symbol size and have not been displayed here for visual clarity, however glass and parafilm results agree to within experimental error.
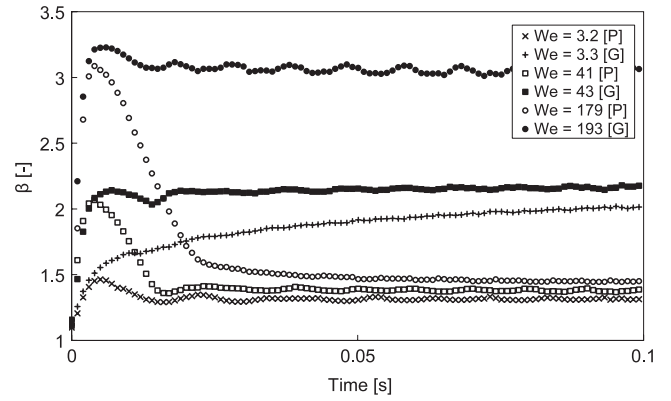

Figure 13. Dimensionless drop diameter β plotted against time for drops of the X050 shear-thinning fluid ($K = 2.846$ Pa s^n, $n = 0.129$) impacting from fall heights of 10 ($We \sim 3$), 50 ($We \sim 42$) and 200 mm ($We \sim 185$) on glass [G] (solid symbols) and parafilm-M [P] (open symbols) substrates.
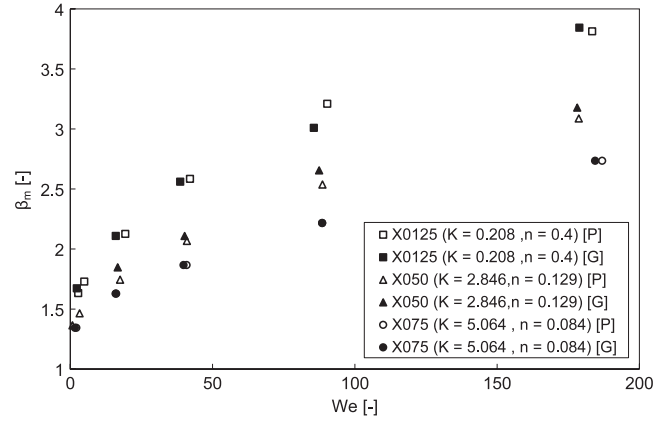

Figure 12. Comparison of the minimum dimensionless height factor ξ_m for Newtonian fluid drops GLY098 ($\mu = 0.925$ Pa s, $D_E = 3.102$ mm), GL094 ($\mu = 0.428$ Pa s, $D_E = 3.101$ mm) and GLY080 ($\mu = 0.056$ Pa s, $D_E = 3.133$ mm) impacting on parafilm [P] ($\theta_e = 95° \pm 2°$, open symbols) and glass [G] ($\theta_e = 0°$, solid symbols) substrates. Errors are predominantly comparable to the symbol size and have not been displayed here for visual clarity, however glass and parafilm results agree to within experimental error.
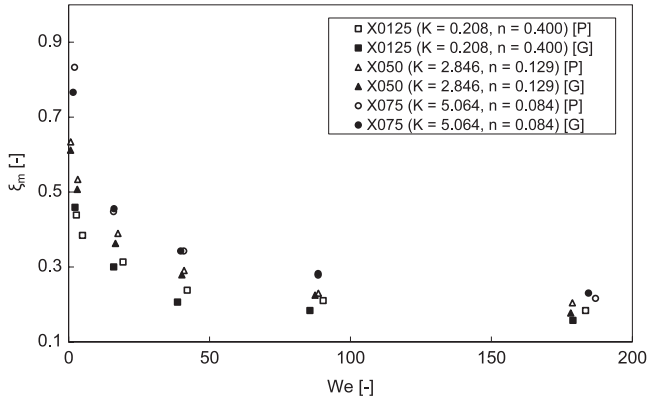

Figure 14. Comparison of the dimensionless diameter β_m at the end of inertial expansion for shear-thinning fluid drops X0125 ($K = 0.208$ Pa s^n, $n = 0.400$, $D_E = 3.474$ mm), X050 ($K = 2.846$ Pa s^n, $n = 0.129$, $D_E = 3.428$ mm) and X075 ($K = 5.064$ Pa s^n, $n = 0.084$, $D_E = 3.347$ mm) impacting on parafilm [P] (open symbols) and glass [G] (solid symbols) substrates. Errors are predominantly comparable to the symbol size and have not been displayed here for visual clarity, however glass and parafilm results agree to within experimental error.

measurements show the opposite trend: β_m increases for less shear-thinning fluids. This suggests that whilst shear-thinning effects may influence the impact behaviour, the influence of the consistency coefficient K appears to dominate.

An alternative perspective can be achieved by modelling the viscous characteristics of the shear-thinning fluids in terms of the Cross model (3). This model characterizes shear-thinning properties using a dynamic viscosity range ($\mu_0 - \mu_1$). During impact, a shear-thinning drop exhibiting axisymmetric spreading (with a central stagnation point) will produce a range of viscosities between μ_0 and a minimum μ' where $\mu_1 \leqslant \mu'$. For high velocity impacts where shear-rates are very large, μ'

is expected to be similar to μ_0. From table 5, increasing the mass fraction of xanthan gum increases the dynamic viscosity range, primarily by increasing μ_0. For two drops subject to equivalent impacts therefore, the higher mass fraction fluid will exhibit larger average viscosities within the fluid. This results in decreases of β_m in a similar fashion to increasing μ for the Newtonian fluids.

The analysis of shear-thinning fluid drops during impact is made increasingly complex because fluid viscosity is not constant and varies as a function of the shear rate, which itself varies both with radial position in the drop and time. Newtonian prediction models that characterize impact behaviour using the Reynolds, the Ohnesorge and the Capillary numbers cannot therefore be easily modified to predict shear-thinning fluid behaviour without losing their original simplicity and requiring iterative methods to obtain a

Table 5. Cross model parameters for shear-thinning fluids.

Shear-thinning solution	C (s)	μ_0 (Pa s)	μ_1 (Pa s)	m (—)	R^2 fit
X0125	1.9822 ± 0.327	0.597 ± 0.068	0.0048 ± 0.00083	0.23666 ± 0.025	0.99841
X075	2.7452 ± 0.004	14.436 ± 0.417	0.0068 ± 0.00081	0.0648 ± 0.0032	0.99998

Figure 15. Comparison of the dimensionless apex height ξ_m at the end of inertial expansion for shear-thinning fluid drops X0125 ($K = 0.208$ Pa s^n, $n = 0.400$, $D_E = 3.474$ mm), X050 ($K = 2.846$ Pa s^n, $n = 0.129$, $D_E = 3.428$ mm) and X075 ($K = 5.064$ Pa s^n, $n = 0.084$, $D_E = 3.347$ mm) impacting on parafilm [P] (open symbols) and glass [G] (solid symbols) substrates. Errors are predominantly comparable to the symbol size and have not been displayed here for visual clarity, however glass and parafilm results agree to within experimental error.
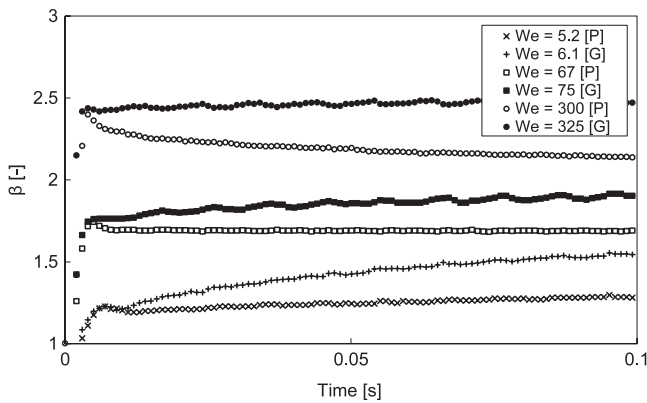

Figure 16. Dimensionless drop diameter β plotted against time for drops of the YSF030 viscoplastic fluid ($K = 5.533$ Pa s^n, $n = 0.3775$, $\tau_c = 11.5$ Pa) impacting from fall heights of 10 ($We \sim 5.5$), 50 ($We \sim 70$) and 200 mm ($We \sim 315$) on glass [G] (solid symbols) and parafilm-M [P] (open symbols) solid substrates.

solution. Predictions of shear-thinning drop impact behaviour for fluids with varying K and n cannot therefore be easily determined. This further limits the amount of experimental analyses that can be completed. Qualitatively however, some effects of fluids shear-thinning can be examined: for each shear-thinning fluid (figure 14), β_m, is typically much larger than those observed for the Newtonian fluids (figure 11). The consistency coefficient K provides an indication of the maximum fluid viscosity that the fluid exhibits; this ranges
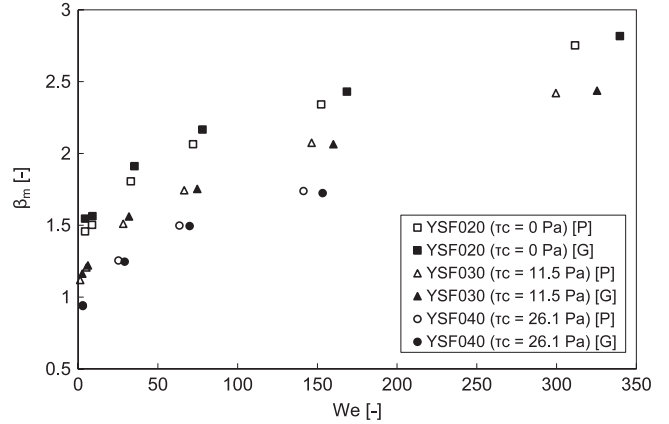

Figure 17. Comparison of β_m at the end of inertial expansion for viscoplastic fluid drops YSF020 ($K = 1.443$ Pa s^n, $n = 0.4747$, $\tau_c = 0$ Pa, $D_E = 2.848$ mm), YSF030 ($K = 5.533$ Pa s^n, $n = 0.3775$, $\tau_c = 11.5$ Pa, $D_E = 2.678$ mm) and YSF040 ($K = 7.936$ Pa s^n, $n = 0.3727$, $\tau_c = 26.1$ Pa, $D_E = 2.617$ mm) impacting on parafilm [P] (open symbols) and glass [G] (solid symbols) substrates. Errors are predominantly comparable to the symbol size and have not been displayed here for visual clarity, however glass and parafilm results agree to within experimental error.
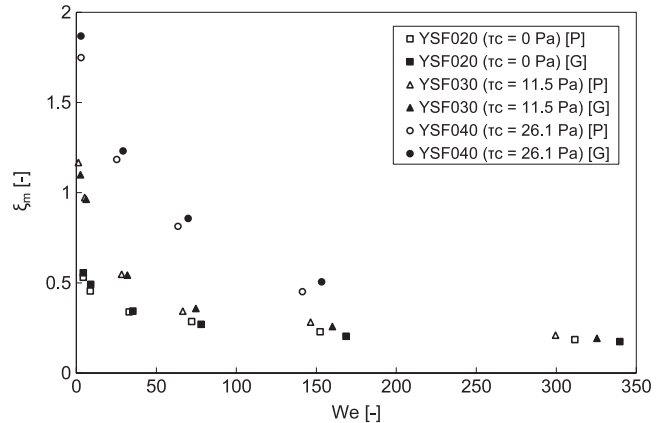

Figure 18. Comparison of ξ_m at the end of inertial expansion for viscoplastic fluid drops YSF020 ($K = 1.443$ Pa s^n, $n = 0.4747$, $\tau_c = 0$ Pa, $D_E = 2.848$ mm), YSF030 ($K = 5.533$ Pa s^n, $n = 0.3775$, $\tau_c = 11.5$ Pa, $D_E = 2.678$ mm) and YSF040 ($K = 7.936$ Pa s^n, $n = 0.3727$, $\tau_c = 26.1$ Pa, $D_E = 2.617$ mm) impacting on parafilm [P] (open symbols) and glass [G] (solid symbols) substrates. Errors are predominantly comparable to the symbol size and have not been displayed here for visual clarity, however glass and parafilm results agree to within experimental error.

between 0.208 Pa s$^n \leqslant K \leqslant 5.064$ Pa s^n for the four shear-thinning fluids. The X075 ($K = 5.064$ Pa s^n) fluid can exhibit much larger viscosities than the most viscous GLY098
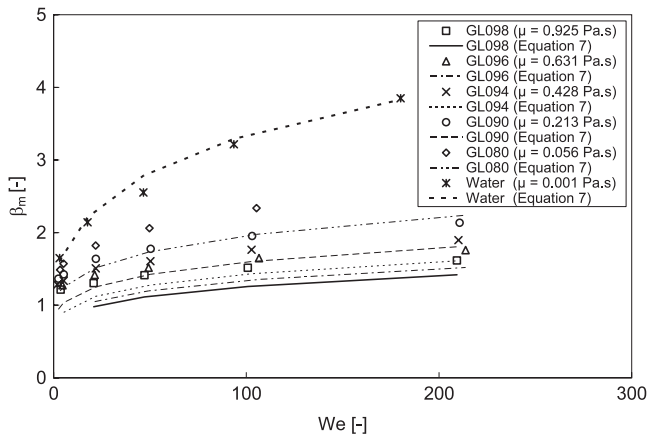
Figure 19. Comparison of D_{Max}/D_E for Newtonian glycerol solutions GL098 (square), GL096 (triangle), GL094 (diamond), GL090 (cross) and GL080 (circle) with theoretical predictions from (7).
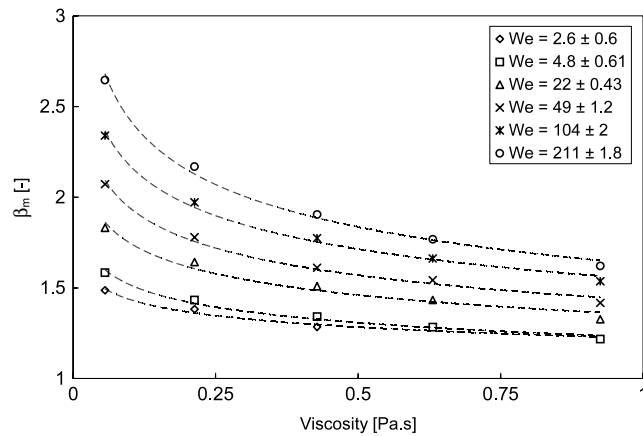

Figure 21. Temporal variations in β and ξ for drops of the four shear-thinning fluids ($0.084 \leqslant n \leqslant 0.400$, 0.208 Pa s^n $\leqslant K \leqslant 5.064$ Pa s^n) impacting from $H_f = 50$ mm ($We = 43.2 \pm 1.4$) on a parafilm substrate.

Figure 20. Power law distributions (dashed lines) fitted to D_{Max}/D_E (symbols) plotted against μ for Newtonian fluid drop impacts with $We = 2.6 \pm 0.6$ (diamond), $We = 4.8 \pm 0.61$ (square), $We = 22 \pm 0.43$ (triangle), $We = 49 \pm 1.2$ (cross), $We = 104 \pm 2$ (star) and $We = 211 \pm 1.8$ (circle).

Figure 22. D_{Max}/D_E plotted against τ_c for viscoplastic fluid drops impacting on a parafilm-M substrate with $We = 5.6 \pm 2$ (square), $We = 29 \pm 3$ (diamond), $We = 68 \pm 3$ (triangle), $We = 146 \pm 4$ (circle) and $We = 303 \pm 6$ (star). The dashed lines correspond to a linear least square best fit. Errors margins are comparable to the symbol size and have not been displayed for visual clarity.

Newtonian fluid ($\mu = 0.925$ Pa s), however values of β_m at similar Weber numbers are equivalent to the least viscous GLY080 ($\mu = 0.056$ Pa s) Newtonian fluid. This suggests fluid shear-thinning has a significant effect on impact behaviour.

3.4. Influence of yield-stress

Figure 22 displays β_m plotted against yield-stress magnitude for fluids with 0 Pa $\leqslant \tau_c \leqslant 26.1$ Pa impacting on a parafilm substrate within the range $5.6 \leqslant We \leqslant 303$. Whilst β_m is observed to decrease linearly with increasing τ_c for equivalent impacts, the effects of shear-thinning have not been accounted for. As section 3.3 highlights, shear-thinning appears to have a significant influence on drop impact behaviour.

Viscoplastic fluids exhibit both shear-thinning and yield-stress effects. These fluids can most simply be characterized in terms of n, K and τ_c (1). The difficulty in separating the independent effects of n and K for the shear-thinning fluids however suggests that an additional yield-stress term would further complicate matters. Indeed it is not possible to
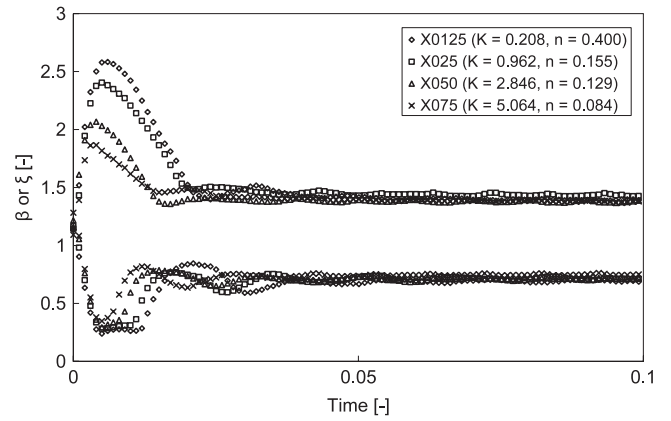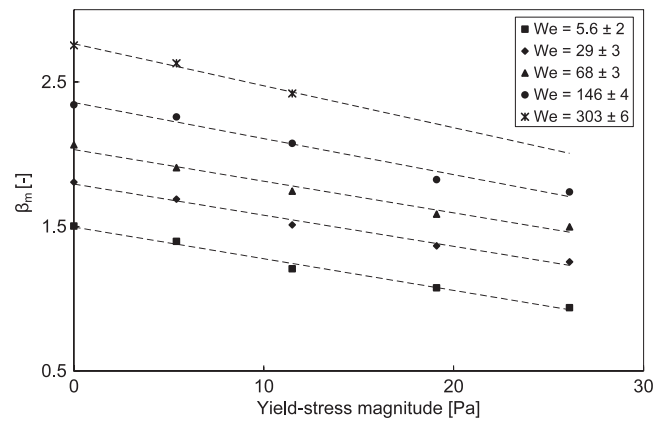
determine the independent influence of yield-stress on impact dynamics by direct comparison of experimental results because it is not possible to produce fluids with identical shear-thinning properties and differing yield-stress magnitudes. One aspect that can be further scrutinized however is the presence of peaks. Neither shear-thinning or Newtonian fluid drops exhibit this morphological characteristic during impact, therefore it is considered entirely related to viscoplasticity.

The presence of drop peaks can clearly be observed in figure 18. Across the range $2.9 \leqslant We \leqslant 340$, the maximum variation in ξ_m is small for the YSF020 solution ($\tau_c = 0$ Pa, $\Delta\xi_m = 0.35$); similar magnitude variations are also observed for the Newtonian ($0.27 \leqslant \Delta\xi_m \leqslant 0.47$ for $0.056 \leqslant \mu \leqslant 0.925$ Pa s) and shear-thinning fluids ($0.25 \leqslant \Delta\xi_m \leqslant 0.62$ for 0.208 Pa s^n $\leqslant K \leqslant 5.064$ Pa s^n, $0.084 \leqslant n \leqslant 0.4$) across similar ranges in We. Height differences increase significantly however with increasing τ_c; the maximum difference for the YSF040 solution ($\tau_c = 26.1$ Pa) is $\Delta\xi_m = 1.3$ over $3 \leqslant We \leqslant 141$. This value exceeds unity and is due to the presence of
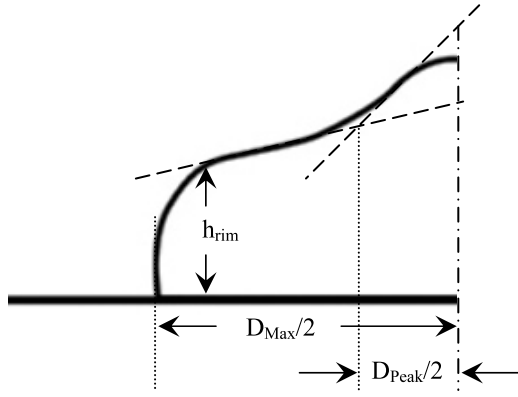
Figure 23. Determination of drop peak diameter D_T/D_{Max} measuring the intersection of surface tangents at the inflection points.
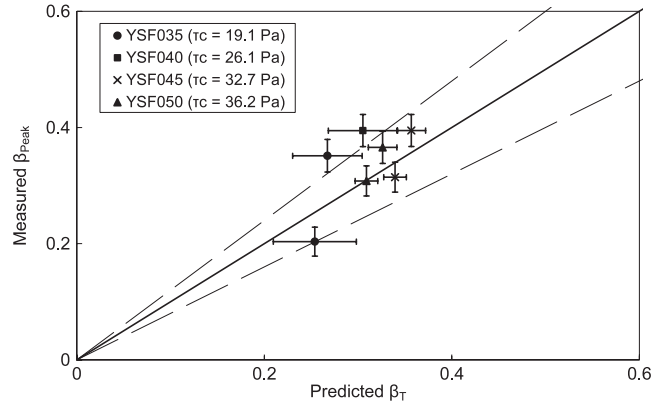

Figure 24. Measured drop peak diameter β_{Peak} plotted against predicted threshold diameter β_T (denoting the perimeter inside which shear-stresses during impact are smaller than the yield-stress) for yield-stress fluid drops with 19.1 Pa $\leqslant \tau_c \leqslant$ 36.2 Pa impacting on a parafilm substrate within the range $67 \leqslant We \leqslant 203$.

a central peak in the drop, visible in figures 6 and 9. The presence of peaks comes from incomplete drop deformation during impact; the upper region of impacting drops do not significantly deform from their original prolate shape during free-fall. For impacts at similar We, peak heights increase with τ_c. Moreover, for low velocity impacts ($H_f = 10$ mm) of fluids with $\tau_c \geqslant 11.5$ Pa, inertial deformation is so small that peaks account for most of the drop volume. This suggests that in addition to shear-thinning effects influencing drop impact behaviour, radial flow will be inhibited within a threshold radius where shear-stresses arising during impact fall below the yield-stress magnitude.

Dimensionless drop peak diameters, $\beta_{Peak} = D_{Peak}/D_{Max}$, are determined by measuring the intersection of the drop peak and lamella surface tangents (taken at the inflection pints of drop contours), as shown in figure 23. Measurable drop peaks are present after impacts of the YSF035 and YSF040 fluids for $H_f \leqslant 100$ mm and for the YSF045 and YSF050 fluids for $H_f \leqslant 150$ mm. Whilst peaks exist at low fall heights for each of these solutions, drop deformation is small and surface tangent intersections and drop heights at the rim cannot be accurately measured. Moreover, complete drop deformation is observed for fluids with $\tau_c \leqslant 19.1$ Pa over the full range of We.

To establish a relationship between peak diameter and yield-stress magnitude, measured values of β_{Peak} are compared with a theoretical threshold diameter, $\beta_T = D_T/D_{Max}$, where D_T is defined as the diameter where shear-stresses arising in the lamella during inertial spreading equal the yield-stress magnitude of the fluid. During the expansion phase, the radial velocity, v_x, will be at a maximum close to the lamella rim [33]. The maximum shear rate and shear-stress can therefore be approximated respectively by

$$\dot{\gamma}_{Max} \approx \left. \frac{v_{x\,max}}{h_{rim}(x)} \right|_{R_{Max}} \tag{8}$$

and

$$\tau_{Max} = \tau_c + K\dot{\gamma}^n = \tau_c + K \left. \left(\frac{v_{x\,max}}{h_{rim}(x)} \right)^n \right|_{R_{Max}} \tag{9}$$

where h_{rim} (R_{Max}) is the lamella height at the rim ($R_{Max} = D_{Max}/2$), x is the Cartesian coordinate in the radial direction and the viscosity term has been replaced by a Herschel–Bulkley model. v_x will vary with time during the impact process, therefore this term represents the maximum average radial velocity during inertial spreading. This is used to provide an upper limit to the shear rate and stress terms. For each drop, v_x is directly extracted from measurements.

Whilst it is not known how the radial velocity, shear-rates or shear-stresses vary across the lamella during impact, upon assuming the deforming drop has rotational symmetry about the vertical axis, each of these terms will decrease from a maximum near the rim to zero at the lamella centre. As a first approximation, we assume this variation to be linear. The dimensionless threshold diameter β_T can therefore be defined where $\tau = \tau_c$ so that:

$$\beta_T = \frac{D_T}{D_{Max}} = \frac{\tau_c}{\tau_{Max}} = \frac{\tau_c}{\tau_c + K \left. \left(\frac{v_{r\,max}}{h_r(x)} \right)^n \right|_{D_{Max}/2}}. \tag{10}$$

Within the perimeter defined by this diameter, shear-stresses are too small to cause deformation during impact and the drop shape remains undeformed, resulting in a drop peak.

Figure 24 compares β_T with measured values of β_{Peak}. Predictions are confined within a range limited by an upper level above which inertial forces result in the complete deformation of impacting drops (such that no central peak is observed) and a lower limit below which drops show only small deformations and measured values of drop rim height cannot be measured.

The similarity of the predicted threshold diameters with those of the measured drop peak sizes appears to confirm the hypothesis that fluid yield-stress influences drop impact dynamics by inhibiting fluid motion within a definable region during the expansion phase. Predictions also highlight that the threshold region varies in size both with τ_c and the Weber number. As the Weber number increases, the maximum shear-stresses near the drop rim rise and (based on the approximated linear radial variation of shear-stress from the centre to the

lamella edge) the threshold region of yield-stress influence decreases in size, eventually resulting in complete deformation of the impacting drop and the disappearance of the drop peak. Observed changes in measured drop peak sizes confirm these trends. Whilst yield-stress effects may continue to influence inertial spreading behaviour for higher velocity impacts where drops completely deform and peaks are no longer present, this cannot be established from the analysis. Moreover, larger drop peak sizes are observed for equivalent impacts of fluids with increasing τ_c, indicative of an increase in the threshold diameter with increased τ_c.

4. Conclusions

A systematic investigation of non-Newtonian drops impacting onto a horizontal solid substrate was carried out characterize the impact morphology as compared with drops of Newtonian fluids. In particular, drops of shear-thinning and yield-stress fluids impacting on substrates of different surface energies were compared to Newtonian drops of different viscosities.

The impact morphology of shear-thinning drops is qualitatively similar to that of Newtonian drops. From a quantitative point of view, if the fluid is described with a power law constitutive model one can observe a small but measurable effect of the shear-thinning exponent on the spreading diameter and the lamella thickness. However, the influence of the consistency coefficient appears to dominate.

More interesting is the impact morphology of yield-stress drops. In particular, the most interesting feature of these drops is the presence of characteristic peaks in the centre of the lamella, which can be observed even when drop spreading is complete. Such peaks arises due to both the highly prolate equilibrium drop shape of some viscoplastic fluids during free-fall and the incomplete deformation during the expansion phase (resulting in drops having a deformed outer region, similar in appearance to a typical lamella and an undeformed inner region). Measured drop peak diameters, were compared with predictions of a threshold diameter where shear-stresses (which vary from zero at the axisymmetric drop centre to a maximum at the lamella rim) equal the yield-stress magnitude. Predictions are in good agreement with measurements, supporting the hypothesis that close to the drop centre, where shear-stresses are greatly reduced, the fluid remains locally undeformed.

Acknowledgment

References

[1] Bertola V 2008 Some applications of controlled drop deposition on solid surfaces *Recent Patents Mech. Eng.* **1** 167–74
[2] Chandra S and Avedisian C T 1991 On the collision of a droplet with a solid surface *Proc. R. Soc.* A **432** 13
[3] Rein M 1993 Phenomena of liquid-drop impact on solid and liquid surfaces *Fluid Dyn. Res.* **12** 61
[4] Yarin A L 2006 Drop impact dynamics: splashing, spreading, receding, bouncing *Annu. Rev. Fluid Mech.* **38** 159
[5] De Gennes P G 1985 Wetting—statics and dynamics *Rev. Mod. Phys.* **57** 827–63
[6] Clanet C, Beguin C and Richard D 2004 Maximal deformation of an impacting drop *J. Fluid Mech.* **517** 199
[7] Crooks R and Boger D V 2000 Influence of fluid elasticity on drops impacting on dry surfaces *J. Rheol.* **44** 973–96
[8] Crooks R, Cooper-Whitez J and Boger D V 2001 The role of dynamic surface tension and elasticity on the dynamics of drop impact *Chem. Eng. Sci.* **56** 5575–92
[9] Bergeron V 2003 Designing intelligent fluids for controlling spray applications *C. R. Physique* **4** 211–9
[10] Bertola V 2004 Drop impact on a hot plate: effect of a polymer additive *Exp. Fluids* **37** 653–64
[11] Bertola V and Sefiane K 2005 Controlling secondary atomization during drop impact on hot surfaces by polymer additives *Phys. Fluids* **17** 108104
[12] Bertola V 2009 An experimental study of bouncing Leidenfrost drops: comparison between Newtonian and viscoelastic liquids *Int. J. Heat Mass Transfer* **52** 1786–93
[13] Nigen S 2005 Experimental investigation of the impact of an (apparent) yield-stress material *At. Sprays* **15** 103
[14] Bird R B, Gance D and Yarusso B J 1982 The rheology and flow of viscoplastic materials *Rev. Chem. Eng.* **1** 1–70
[15] Cross M M 1965 Rheology of non-Newtonian fluids: a new flow equation for pseudoplastic systems *J. Colloid Sci.* **20** 417
[16] Scheller B L and Bousfield D W 1995 Newtonian drop impact with a solid-surface *AIChE J.* **41** 1357
[17] Pasandideh Fard M, Qiao Y M and Chandra S 1996 Capillary effects during droplet impact on a solid surface *Phys. Fluids* **8** 650
[18] Mao T, Kuhn D C S and Tran H 1997 Spread and rebound of liquid droplets upon impact on flat surfaces *AIChE J.* **43** 2169
[19] Fukai J, Shiiba Y and Yamamoto T 1995 Wetting effects on the spreading of a liquid droplet colliding with a flat surface—experiment and modeling *Phys. Fluids* **7** 236
[20] Macosko C W 1994 *Rheology Principles, Measurements and Applications* (New York: Wiley–VCH)
[21] Barnes H A 1999 The yield stress—a review or '$\pi\alpha\eta\tau\alpha\rho\varepsilon\iota$'—everything flows? *J. Non-Newton. Fluid Mech.* **81** 133
[22] Coussot P 2007 Rheophysics of pastes: a review of microscopic modeling approaches *Soft Matter* **3** 528
[23] Mittal K L 1972 Determination of CMC of Polysorbate 20 in aqueous-solution by surface tension method *J. Pharm. Sci.* **61** 1334
[24] Dushkin C D and Iliev T H 1994 Dynamic surface tension of micellar solutions studied by the maximum bubble pressure method: 2. Theory of the solutions below C.M.C. *Colloid Polym. Sci.* **272** 1157
[25] Geeraerts G and Joos P 1994 Dynamic surface tension of micellar Triton X-100 solutions *Colloids Surf.* A **90** 149
[26] Dutschk V, Sabbatovskiy K G, Stolz M, Grundke K and Rudoy V M 2003 Unusual wetting dynamics of aqueous surfactant solutions on polymer surfaces *J. Colloid Interface Sci.* **267** 456
[27] Range K and Feuillebois F 1998 Influence of surface roughness on liquid drop impact *J. Colloid Interface Sci.* **203** 16
[28] Stow C D and Hadfield M G 1981 An experimental investigation of fluid-flow resulting from the impact of a water drop with an unyielding dry surface *Proc. R. Soc.* A **373** 419

[29] Attané P, Girard F and Morin V 2007 An energy balance approach of the dynamics of drop impact on a solid surface *Phys. Fluids* **19** 012101

[30] Bertola V 2009 Wicking with a yield-stress fluid *J. Phys.: Condens. Matter* **21** 035107

[31] Chandra S and Avedisian C T 1991 On the collision of a droplet with a solid surface *Proc. R. Soc.* A **432** 13

[32] German G and Bertola V 2009 A review of drop impact models and validation with high-viscosity Newtonian fluids *At. Sprays* at press

[33] Roisman I V, Rioboo R and Tropea C 2002 Normal impact of a liquid drop on a dry surface: model for spreading and receding *Proc. R. Soc.* A **458** 1411